THE JOURNAL OF PHYSICAL CHEMISTRY C

Article

pubs.acs.org/JPCC

Zn-Doped Fe_3O_4 Nanosheet Formation Induced by EDA with High Magnetization and an Investigation of the Formation Mechanism

Jie Zhu and Zhaodong Nan*

College of Chemistry and Chemical Engineering, Yang Zhou University, 225002 Yangzhou, People's Republic of China

Supporting Information

ABSTRACT: Ethylenediamine (EDA) was always used as an additive to modify nanomaterial formation. However, the effect of EDA on the nanomaterial formation process has not been studied in detail. In the present study, Zn-doped Fe_3O_4 magnetic nanosheets with a high magnetization and surface area were synthesized by a facile one-step solvothermal method, where EDA was added to the reaction system. The formation mechanism was first studied in detail by using an in situ calorimetric method. Compared to Zn-doped Fe_3O_4 clusters synthesized by the same method without EDA, the complex formation, as $[Fe(EDA)_3]^{3+}$ and $[Zn(EDA)_3]^{2+}$, prevented alkoxide ($Fe_2(C_2H_4O_2)_3$ and $ZnC_2H_4O_2$) formation and resulted in some reactions occurring at higher temperature. At the same time, the (111) facets of Zn-doped Fe_3O_4 became stable, which resulted in nanosheet formation. And the effect of EDA on the magnetization of the sample can be explained by the Zn^{2+} distributions at the tetrahedral (A site) and octahedral (B site) sites. These results demonstrated further that the EDA can change the Zn-doped Fe_3O_4 formation mechanism, which has not been reported before as we know.

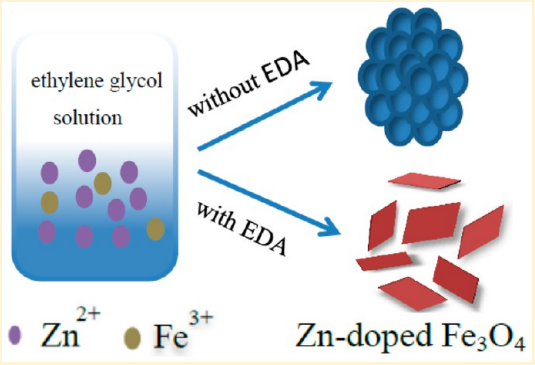

INTRODUCTION

Magnetic nanoparticles have received increasing attention in past decades. Among these magnetic nanoparticles, ferrite magnetic nanoparticles have been extensively investigated owing to their wide use in different fields,[1−5] in which the fabrication of monodisperse nanoparticles with high magnetization and surface area simultaneously is critical for the application.[6] Nanosized magnetic materials usually show a low magnetization value because of small particles, which limits their practical applications. The magnetization can be enhanced through increasing particle size,[7,8] which usually induces a superparamagnetic−ferrimagnetic transition.

Zinc is one of the commonly used metal dopants into Fe_3O_4 because of its nonmagnetic property. Zn ferrite is an important spinel ferrite with excellent physical properties, and its properties are crucially determined by the size, morphology, and cation distribution.[9] A series of Zn ferrite nanoparticles were synthesized by using a chemical coprecipitated technique in which $Zn_{0.2}Fe_{2.8}O_4$ showed a maximum saturation magnetization of 80.93 emu/g.[10]

EDA has been considered to be one of the additives to modify the morphology and magnetic property of ferrites. The fabrication of functional nanoparticles with controllable size and shape is of great importance for their fundamental scientific significance and broad technological applications.[11,12] Ding et al. successfully synthesized Fe_3O_4 nanorods using EDA, which exhibited ferromagnetic behavior at room temperature with a magnetic saturation value of 72.94 emu/g.[13] Hollow spheres of Fe_3O_4 were synthesized with EDA, which show a high saturation magnetization of ca. 68 emu/g.[14] The action of EDA was always reported as similar to that of a surfactant to stable nucleation and some facets of samples. However, no result has not been reported on how to change the material formation mechanism with EDA in detail as far as we know.

In our previous experiment, a series of Zn-doped ferrites was synthesized with cluster-shaped morphology to enhance the magnetization.[15−17] In the present study, EDA was added to the reaction systems. Compared to the Zn-doped Fe_3O_4 synthesized without EDA, the morphology of the as-prepared sample changed significantly from cluster to monodispersed nanosheets, and the magnetization was obviously enhanced. At the same time, the as-prepared sample had a higher BET surface area (80.6 m^2/g), which can be widely used in different fields. Thus, it is very interesting to study ferrite formation with EDA. The formation mechanism of the nanosheet-shaped ferrite was studied in detail by in situ calorimetry. The results demonstrated that EDA induced the (111) facet of the sample to be stable and significantly changed the Zn-doped Fe_3O_4 magnetic nanosheet formation mechanism.

EXPERIMENTAL SECTION

Materials. All chemicals in this work, such as ferric nitrate nonahydrate ($Fe(NO_3)_3{\cdot}9H_2O$), zinc nitrate hexahydrate ($Zn(NO_3)_2{\cdot}6H_2O$), ethylene glycol ($C_2H_6O_2$), sodium eth-

Received: March 4, 2017
Revised: April 17, 2017
Published: April 19, 2017

DOI: 10.1021/acs.jpcc.7b02084
J. Phys. Chem. C 2017, 121, 9612−9620

oxide (C_2H_5ONa), and ethylenediamine ($C_2H_8N_2$), were analytical-grade regents from the Sinopharm Chemical Reagent Company and were used as starting materials without further purification.

Synthesis of Zn-Doped Fe_3O_4 Magnetic Nanosheets. In a typical experiment, 0.60 mmol of $Zn(NO_3)_2{\cdot}6H_2O$ and 8.4 mmol of ($Fe(NO_3)_3{\cdot}9H_2O$) were dissolved in 25 mL of anhydrous ethylene glycol, for which the molar ratio of Zn^{2+} to Fe^{3+} was 1/14. Then, 9.0 mmol of CH_3COONa was added to the solution. The whole mixture was stirred vigorously to give a homogeneous solution, followed by the addition of ethylenediamine (EDA) in different molar amounts. Subsequently, the solution was transferred to a 50 mL Teflon-lined stainless steel autoclave, which was thermally treated for 24 h at 200 °C and then naturally cooled to room temperature. The final product was obtained by washing the precipitate a few times with distilled water and ethanol before being dried in a vacuum oven at 50 °C for 24 h. Different samples named E5, E8, E10, E15, and E20 were synthesized with 45, 72, 90, 135, and 180 mmol of EDA, respectively, in which 5, 8, 10, 15, and 20 represent the molar ratio of EDA to metal ions (9.0 mmol of Zn^{2+} and Fe^{3+}).

Characterization. X-ray powder diffraction (XRD) measurements were performed on a Bruker D8 Advance X-ray diffractometer with Cu Ka radiation (l = 1.5418 Å). The 2θ range used in the measurement was from 10 to 80°. Standard and high-resolution transmission electron microscopy (TEM and HRTEM) measurements were performed on a JEOL-2010 TEM at an acceleration voltage of 200 kV. Samples were first ultrasonically dispersed in absolute alcohol and dropcast onto copper grids. Infrared spectrum (FT-IR) measurements were performed on a Nicolet Aexus 470, with scanning from 4000 to 400 cm^{-1} by using KBr pellets under ambient temperature. The metal ion concentration was measured by inductively coupled plasma−atomic emission spectroscopy (ICP−AES) on an Optima 7300 DV (PerkinElmer). The chemical composition of the sample was determined by the dissolution of 0.2200 g of the sample in 10 mL of 28 wt % HCl solution, followed by diluting it to 1000 mL. X-ray photoelectron spectroscopy (XPS) measurements were performed using a Thermo VG Thermo Scientific Escalab 250 fitted with a monochromatized X-ray Al Ka (1486.8 eV) source. A 150 W X-ray spot of 500 mm diameter was used for survey scans. Charge neutralization was accomplished by low-energy electron flooding. All spectra were referenced to the C 1s peak at 284.8 eV. Thermogravimetric analysis (TGA) was performed under argon flow from 50 to 800 °C using a Netzsch ST9449 thermogravimetric analyzer. N_2 adsorption−desorption measurements were carried out on an Omnisorp 100 CX gas adsorption analyzer from Coulter Co to determine the BET surface area. Every sample was degassed at 350 °C for 12 h under a pressure of 10^{-5} Pa or below. The calorimetric experiment was performed using a C-80 microcalorimeter produced by SETARAM (France) with a sensitivity of 0.10 mW.

RESULTS AND DISCUSSION

Structural Analysis. The structures of the samples synthesized by varying the contents of EDA were investigated by using XRD as shown in Figure 1, in which a cubic spinel structure was synthesized and no impurity peaks were observed. The lattice parameter, cell volume, and crystallite size were determined by indexing the XRD patterns, and they are listed in Table 1, where the crystallite size was calculated on the basis of the Debye−Scherrer formula for the strongest (311) diffraction peak. It can be seen from Table 1 that the increasing EDA concentration induced the lattice parameter to increase for E5, E8, E15, and E20 and that the crystallite size increased for E5, E8, E10, and E15. When the molar ratio of EDA to the metal cations was further increased from 15 to 20 for samples E15 and E20, the crystallite size decreased from 18.7 to 18.2 nm. The molar ratios of Zn to Fe determined by ICP-AES for these samples are listed in Table 2. These results demonstrated that the Zn-doped Fe_3O_4 spinel structure was synthesized under the present conditions, and the Zn content was decreased with the EDA increasing from 5 to 15 (molar ratio of EDA to the metal ions) and became higher with EDA further increasing from 15 to 20.

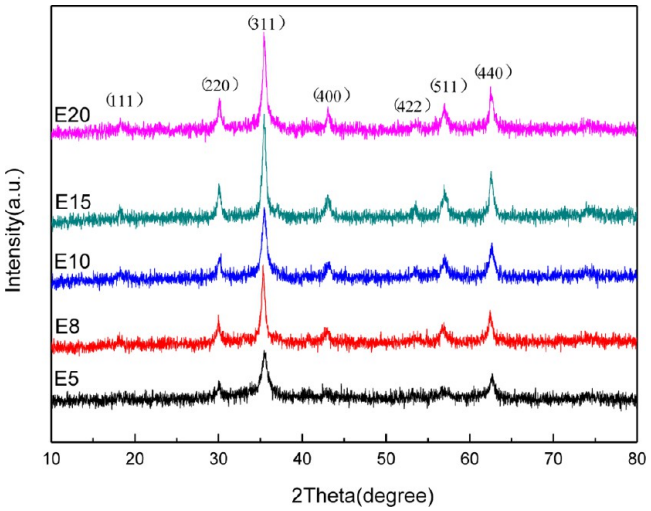

Figure 1. XRD patterns of the samples.

Table 1. Lattice Parameter, Cell Volume, and Crystallite Size of the Samples

sample	lattice parameter (Å)	cell volume (Å^3)	crystallite size (nm)
E5	8.3955	591.8	12.1
E8	8.4250	598.0	13.7
E10	8.5729	630.1	14.6
E15	8.6164	639.7	18.7
E20	8.7262	664.5	18.2

Table 2. Saturation Magnetization (M_s), Remanent Magnetization (M_r), and Coercivities (H_c) of Different Samples as Well as the Molar Ratios of Zn to Fe and Fe^{2+} to Fe^{3+} for the Samples Determined by ICP-AES

sample	M_s (emu/g)	M_r (emu/g)	H_c (Oe)	molar ratio (Zn/Fe)	molar ratio (Fe^{2+}/Fe^{3+})	$Zn_xFe_{3-x}O_4$
E5	64.7	5.48	21.3	0.095	0.368	$Zn_{0.26}Fe_{2.74}O_4$
E8	93.3	13.9	49.5	0.045	0.435	$Zn_{0.13}Fe_{2.87}O_4$
E10	96.6	6.10	23.7	0.042	0.440	$Zn_{0.12}Fe_{2.88}O_4$
E15	119	12.6	47.7	0.030	0.457	$Zn_{0.09}Fe_{2.91}O_4$
E20	70.4	11.1	72.2	0.034	0.451	$Zn_{0.10}Fe_{2.90}O_4$

Fourier transform infrared (FTIR) analysis was performed to identify the structure and the functional groups of the samples as shown in Figure 2. The bands around 3414 and 1621 cm^{-1} were attributed to the O−H stretching vibration and the O−H bending vibration, probably due to the surface water molecules.[18] The bands around 433 and 575 cm^{-1} were

DOI: 10.1021/acs.jpcc.7b02084
J. Phys. Chem. C 2017, 121, 9612−9620

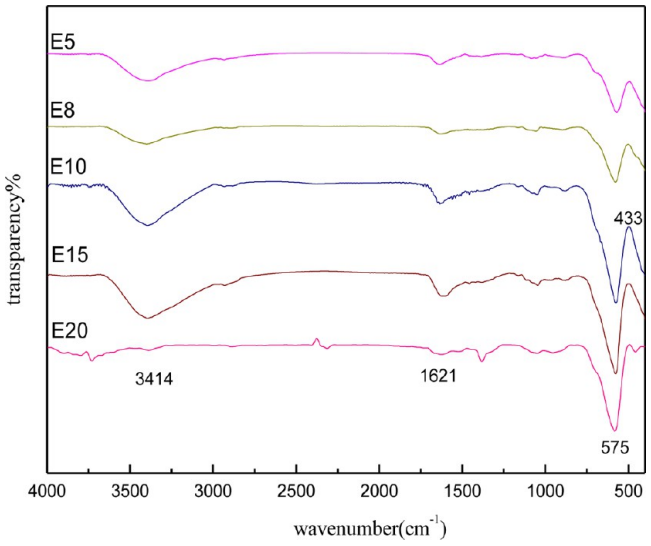

Figure 2. FTIR spectra of the samples.

attributed to the Zn−O vibration and the Fe−O bond vibration, respectively.[19,20] No characteristic peaks of EDA were observed in the spectrum, which indicates the absence of EDA on the surface of the as-prepared samples, which is demonstrated in the following analysis.

The morphology and size of the samples were analyzed through typical TEM images as shown in Figure 3. When no EDA was used, cluster-shaped samples were synthesized with the same method.[15−17] However, no cluster can be seen in Figure 3, which demonstrates that EDA modified the morphology of the sample. Irregular nanoparticles and nanosheets can be seen in Figure 3 for samples E5, E8, and E10, in which the size of the nanoparticles was about 10−20 nm and the length, width, and thickness of these nanosheets were about 20−50, 8−10, and 3−4 nm, respectively. Sample E15 consisted of a large quantity of nanosheets of about the same size as samples E5, E8, and E10. Nanosheets can be seen only for E20 in Figure 3, in which the width of the nanosheets increased to about 30 nm. These results indicate that EDA induced nanosheet formation. Typical HRTEM images of these samples are also shown in Figure 3. The (111) facet with 0.50 nm as the distance between two adjacent planes can be seen clearly for the nanosheets, which indicated that the nanosheet grew along the [111] direction. The selected area diffraction (SAED) pattern of E15 is shown in Figure 4A, which reveals the crystalline nature of ferrite samples, and the diffraction rings are in good consistency with the *hkl* planes present in the cubic spinel structure obtained from XRD. To analyze the purity and elemental composition of E15, energy-dispersive X-ray spectroscopy (EDS) was employed as shown in Figure 4B, which clearly depicts that the as-synthesized sample wis free from any kind of elemental impurity.

Formation Mechanism. Many metallic cations can coordinate with EDA to form stable complexes.[19] Compared to the free cations as reactants, the reaction mechanism may be changed when these complexes are used as reactants. In the present study, E15 was selected to study the formation mechanism by in situ microcalorimetry. A typical microcalorimetric curve is shown in Figure 5. Compared to the microcalorimetric curve without EDA as reported in our previous work,[21] significant differences can be found. Stronger peaks corresponding to the $Fe_2(C_2H_4O_2)_3$, $ZnC_2H_4O_2$,

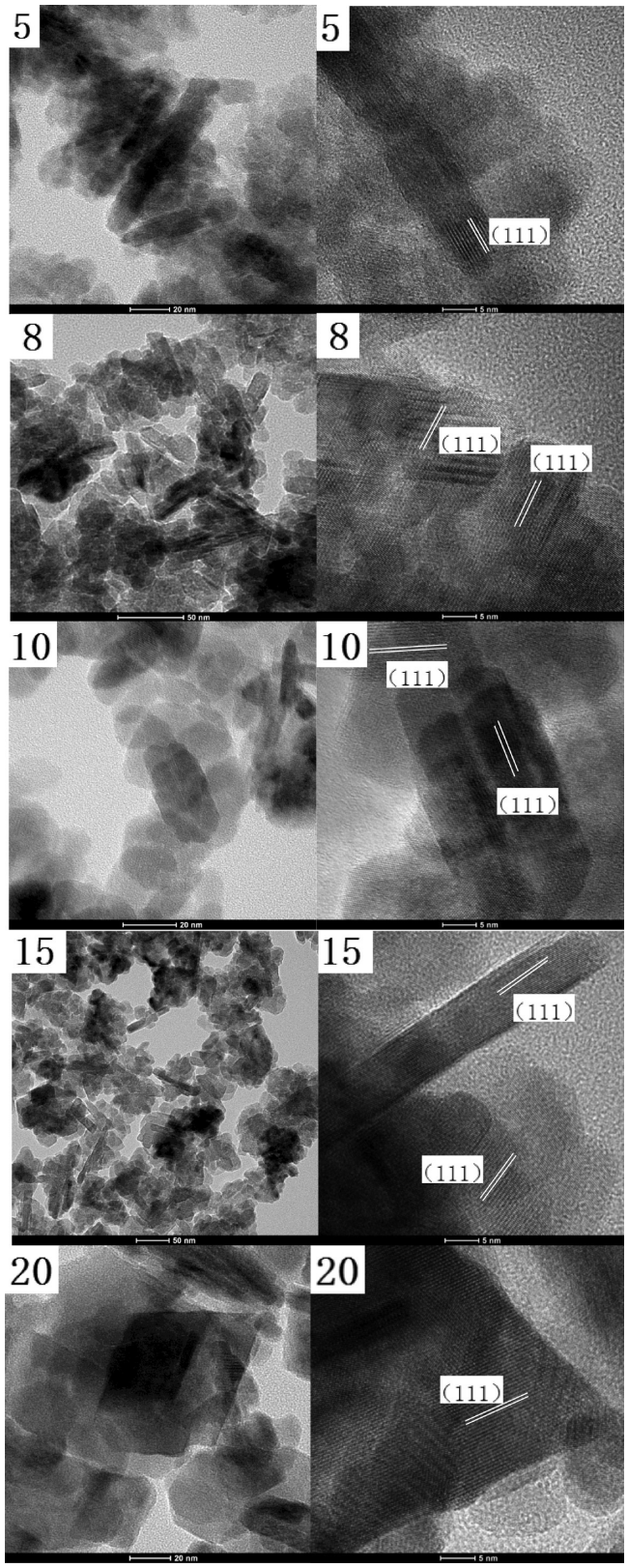

Figure 3. TEM and HRTEM images of the samples, where 5, 8, 10, 15, and 20 represent samples E5, E8, E10, E15, and E20, respectively.

$NaNO_3$, and gel formations were found from room temperature to 150 °C without EDA.[21] Weaker peaks were found only from room temperature to 200 °C in the present system, where the $NaNO_3$ was synthesized at 159 °C as analyzed below, and the

DOI: 10.1021/acs.jpcc.7b02084
J. Phys. Chem. C 2017, 121, 9612−9620

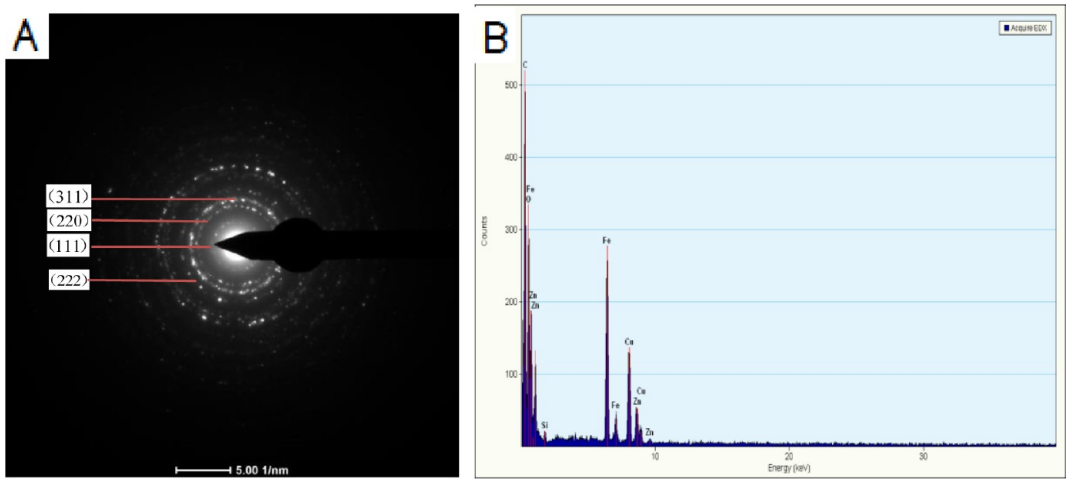

Figure 4. SAED pattern (A) and EDS pattern (B) for sample E15.

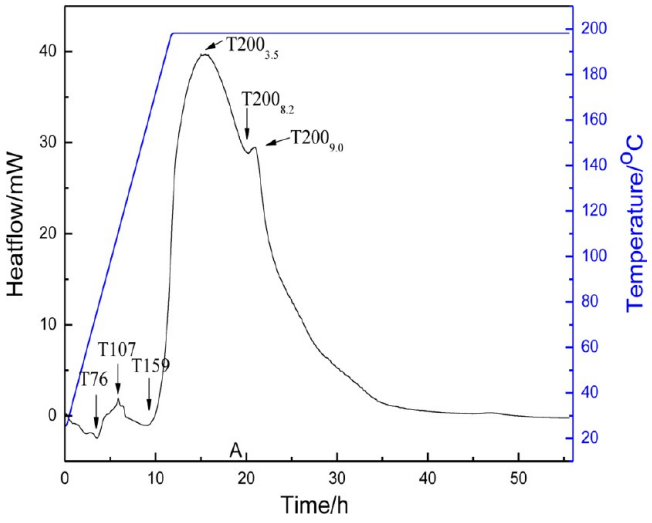

Figure 5. Microcalorimetric curve for sample E15.

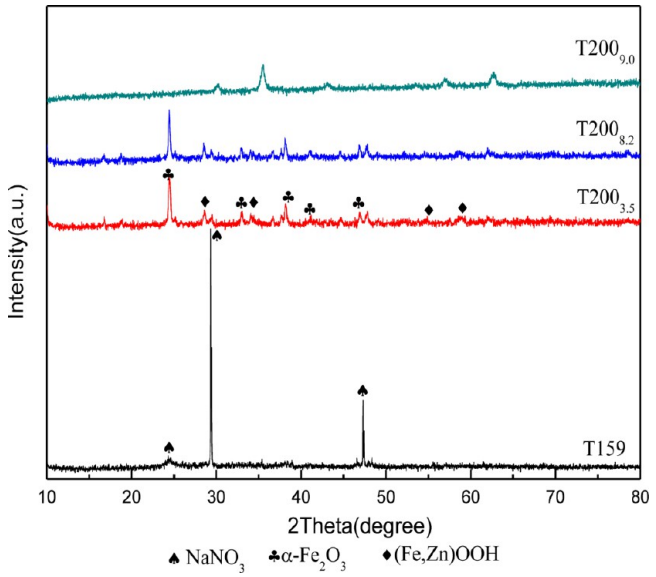

Figure 6. XRD diffraction patterns of the samples synthesized at different reaction temperature and time.

content of $Fe_2(C_2H_4O_2)_3$ and $ZnC_2H_4O_2$ was only about 0.5 wt % as determined by TG as shown in Supporting Information S1. Compared to 13 wt % of the content of $Fe_2(C_2H_4O_2)_3$ and $ZnC_2H_4O_2$ without EDA,[21] the addition of EDA prevented $Fe_2(C_2H_4O_2)_3$ and $ZnC_2H_4O_2$ formation. No gel was found in the present system. These differences indicate that EDA changed the formation mechanism of the Zn-doped ferrite. To further study the formation mechanism, seven samples were selected corresponding to crests and troughs of these peaks as shown in Figure 5. Different samples were named T76, T107, T159, T200$_{3.5}$, T200$_{8.2}$, and T200$_{9.0}$, where 76, 107, 159, and 200 represent the experimental temperatures and subscripts 3.5, 8.2, and 9.0 represent the time (h) kept at 200 °C. No precipitate was found for T76 and T107.

XRD patterns of the solid samples obtained at different reaction temperatures are shown in Figure 6, in which all diffraction peaks of sample T159 were indexed to $NaNO_3$ (ICDD no. 36-1474). The diffraction peaks of samples T200$_{3.5}$ and T200$_{8.2}$ were indexed to α-(Fe, Zn)OOH and α-Fe_2O_3 (ICDD no. 65-0390), and no $NaNO_3$ was found, which was in agreement with the TG results. The diffraction peaks of sample T200$_{9.0}$ were indexed to Fe_3O_4 (ICDD no. 28-0491) and/or $ZnFe_2O_4$ (ICDD no. 22-1012). The molar ratios of Fe to Zn were determined by ICP−AES to be 32.8, 502.6, 128.8, and 34.7 for T159, T200$_{3.5}$, T200$_{8.2}$, and T200$_{9.0}$, respectively. These results indicate that in addition of the $NaNO_3$ crystals, the solid sample consisted of a small amount of amorphous alkoxides $(Fe_2(C_2H_4O_2)_3$ and $ZnC_2H_4O_2$ (about 0.5 wt % based on TG) for T159. α-FeOOH and α-Fe_2O_3 and a small amount of α-$Zn_3(OOH)_2$ were synthesized for T200$_{3.5}$. The α-$Zn_3(OOH)_2$ content increased as the experimental time increased from 3.5 to 8.2 h, in which the molar ratio of Fe to Zn decreased from 502.6 to 128.8. When the experimental time further increased from 8.2 to 9.0 h at 200 °C, a spinel structure was found and the Zn content was significantly increased, which demonstrated that Zn-doped Fe_3O_4 was synthesized.

Fourier transform infrared (FT-IR) analysis was performed to identify the structure and the functional groups of the samples as shown in Figure 7. The bands around 3345 and 1661 cm^{-1} were attributed to the O−H stretching vibration and the O−H bending vibration. The bands around 424 and 536 cm^{-1} were attributed to the Zn−O vibration and Fe−O bond vibration, respectively. For samples T159, T200$_{3.5}$, and T200$_{8.2}$, the two bands around 2871 and 2934 cm^{-1} were attributed to the CH_2-symmetrical stretching vibration and asymmetrical

DOI: 10.1021/acs.jpcc.7b02084
J. Phys. Chem. C 2017, 121, 9612−9620

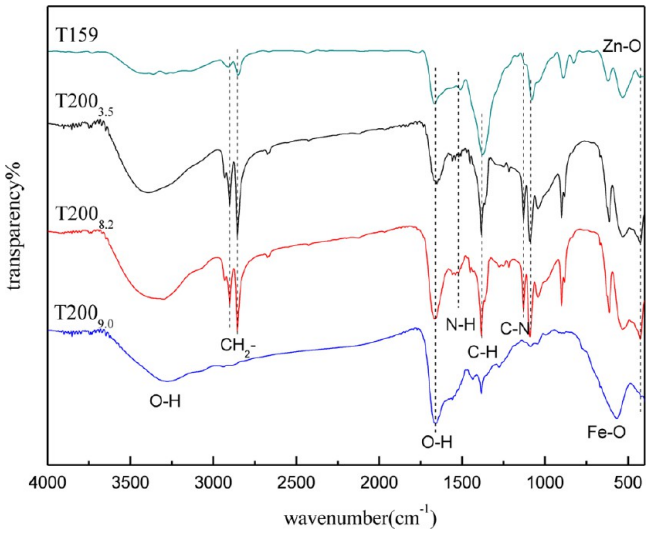

Figure 7. FTIR spectra of the samples synthesized at different reaction temperatures and times.

stretching vibration, respectively. The bands at 1086 and 1130 cm^{-1} are assigned to the C−N stretching vibrations, and the bands around 1382 and 1535 cm^{-1} were attributed to the asymmetric stretching vibrations of the C−H bond vibration and N−H bond vibration, respectively.[22] No band corresponding to EDA was found for $T200_{9.0}$ in Figure 7, which indicated that no EDA was contained in the Zn-doped ferrite based on the XRD.

XPS survey spectra of T159 and $T200_{3.5}$ are shown in Figure 8. Peak values at 1072, 1046.7, 1023.4, 726.1, 712.1, 533.4, 408.4, and 285.2 eV can be indexed to binding energies of Na 1s, Zn $2p_{1/2}$, Zn $2p_{3/2}$, Fe $2p_{1/}2$, Fe $2p_{3/2}$, O 1s, N 1s, and C 1s, respectively, which confirmed the existence of Na, Zn, Fe, O, N, and C elements in the samples. Na 1s was found for $T200_{3.5}$, and no $NaNO_3$ was determined by XRD, which indicated a small amount $NaNO_3$ may be absorbed at the $T200_{3.5}$ surface. Fe^{2+} was determined for $T200_{3.5}$. The details of the XPS analysis are listed in the Supporting Information as Figures S2−S4.

On the basis of the results listed above, a mechanism for Zn-doped Fe_3O_4 formation was proposed. In the beginning, the complex cations were formed as follows:

$$Fe^{3+} + 3EDA \rightarrow [Fe(EDA)_3]^{3+} \quad (1)$$

$$Zn^{2+} + 3EDA \rightarrow [Zn(EDA)_3]^{2+} \quad (2)$$

Compared to Fe^{3+} and Zn^{2+} free ions, $[Fe(EDA)_3]^{3+}$ and $[Zn(EDA)_3]^{2+}$ formation prevented $Fe_2(C_2H_4O_2)_3$ and $ZnC_2H_4O_2$ synthesis. When the experimental temperature increased to 159 °C, $NaNO_3$ crystals and small amounts of $Fe_2(C_2H_4O_2)_3$ and $ZnC_2H_4O_2$ were synthesized.

$$Na^+ + NO_3^- \rightarrow NaNO_3 \quad (3)$$

When Zn-doped Fe_3O_4 was synthesized without EDA,[21] $NaNO_3$ crystals were synthesized at about 99 °C. And the amounts of $Fe_2(C_2H_4O_2)_3$ and $ZnC_2H_4O_2$ were significant higher than those fabricated in the present system. The reason may be that the complex cation formation decreased the free Fe^{3+} and Zn^{2+} concentrations. As a chelating agent, EDA influenced the growth of particles under the hydrothermal reaction.[22] The free Fe^{3+} and Zn^{2+} concentrations dissociated from the complex cations increased as the experimental temperature increased. Small amounts of $Fe_2(C_2H_4O_2)_3$ and $ZnC_2H_4O_2$ were synthesized as the temperature increased to 159 °C.

$$2Fe^{3+} + Zn^{2+} + 4C_2H_6O_2 \rightarrow Fe_2(C_2H_4O_2)_3 + ZnC_2H_4O_2 + 8H^+ \quad (4)$$

At the same time, the following reaction occurred.

$$H^+ + CH_3COO^- \rightarrow CH_3COOH \quad (5)$$

Thus, $NaNO_3$ crystals were formed through the electrostatic interaction between Na^+ and NO_3^-.

As the experimental temperature increased to 200 °C, the hydrolysis of CH_3COO^- and EDA occurred, and OH^- was released. α-(Fe,Zn)OOH and α-Fe_2O_3 were synthesized through the reaction between Fe^{3+} and Zn^{2+} with OH^- as the following, in which eq 7 induced the Zn content decrease. Compared to the reaction at 200 °C, α-(Fe,Zn)OOH and α-Fe_2O_3 were fabricated at 159 °C without EDA.[21]

$$[Fe(EDA)_3]^{3+} + [Zn(EDA)_3]^{2+} + 3OH^- \rightarrow \alpha\text{-(Fe, Zn)OOH} + H_2O + 6EDA \quad (6)$$

$$2\alpha\text{-(Fe, Zn)OOH} + 6EDA \rightarrow \alpha\text{-}Fe_2O_3 + 2[Zn(EDA)_3]^{2+} + H_2O \quad (7)$$

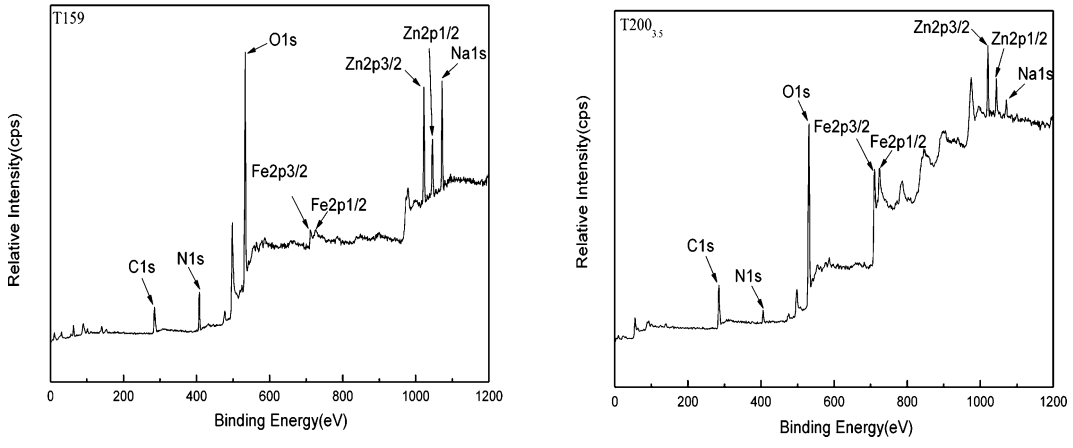

Figure 8. XPS survey spectra of samples T159 and $T200_{3.5}$.

DOI: 10.1021/acs.jpcc.7b02084
J. Phys. Chem. C 2017, 121, 9612−9620

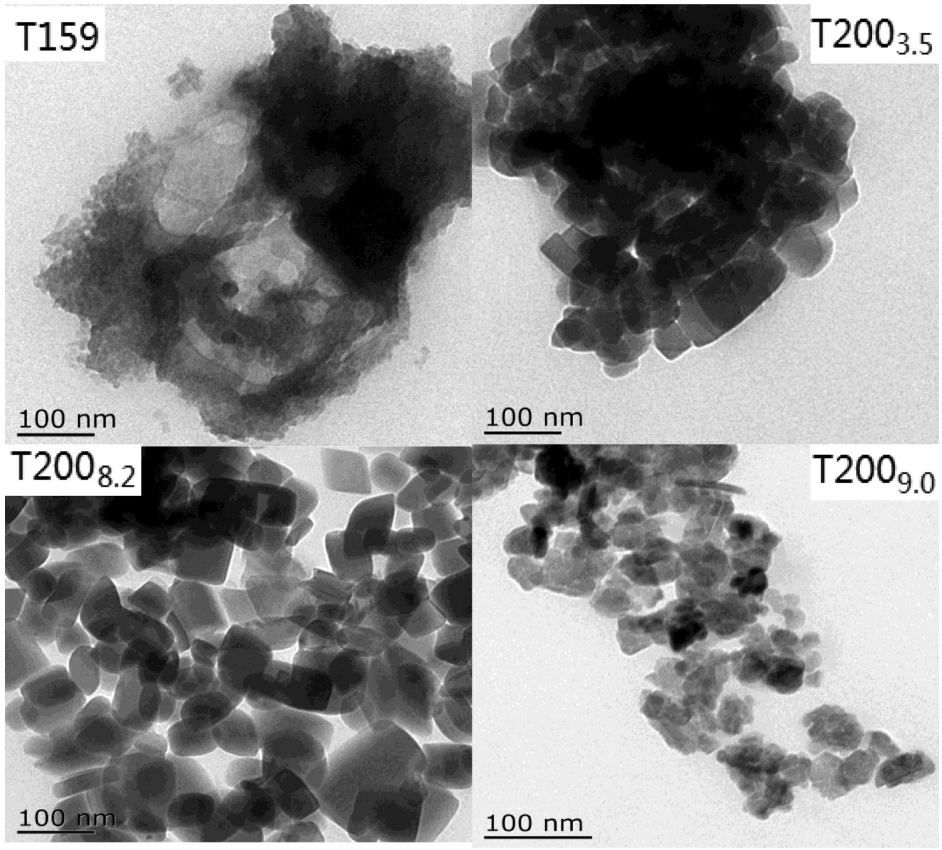

Figure 9. TEM images of the samples.

At the same time, Fe^{2+} was found at 200 °C for 3.5 h through eq 8, which was formed at 159 °C without EDA. Zn-doped Fe_3O_4 crystals were determined at 200 °C for about 9 h, and the Zn content was increased as the experimental time increased according to eq 9.

$$HOCH_2CH_2OH + 6\alpha\text{-}Fe_2O_3 \rightarrow 4Fe_3O_4 + OHCCHO + 2H_2O \quad (8)$$

$$Fe_3O_4 + [Zn(EDA)_3]^{2+} \rightarrow ZnFe_2O_4 + [Fe(EDA)_3]^{2+} \quad (9)$$

Typical TEM images of the samples are shown in Figure 9. For sample T159, nanoparticles were found and amorphous morphology was seen, in which $NaNO_3$ crystals and small amounts of amorphous $Fe_2(C_2H_4O_2)_3$ and $ZnC_2H_4O_2$ were fabricated on the basis of the analysis above. Nanosheets and cube-shaped structures were observed for samples T200$_{3.5}$ and T200$_{8.2}$, in which α-(Fe,Zn)OOH and α-Fe_2O_3 were synthesized. When the experimental time increased from 8.2 to 9.0 h at 200 °C, nanosheets and nanoparticles were found in which Zn-doped Fe_3O_4 crystals were synthesized. When the experimental time further increased to 24 h, almost pure nanosheets were fabricated as shown in Figure 3.

Magnetic Property. The magnetic hysteresis loops of the synthesized samples were measured at room temperature by using a VSM under a maximum applied field from −10 to 10 kOe as shown in Figure 10. The saturation magnetization (M_s), remanent magnetizations (M_r), and coercivities (H_c) are listed in Table 2, and the maximum M_s value is 119 emu/g for E15, which is higher than the reported 80.93 emu/g (for $Zn_{0.2}Fe_{2.8}O_4$ without EDA)[10] and 34.78 emu/g.[22]

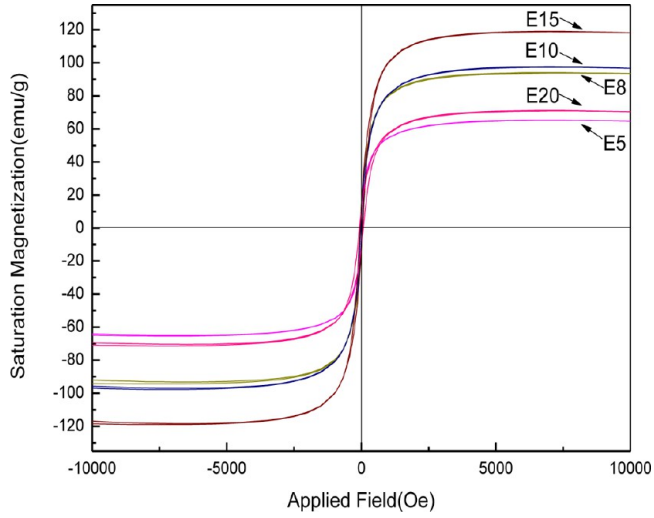

Figure 10. Magnetic hysteresis loops for samples E5−E20.

To explain the M_s change, molar ratios of Fe^{2+} to Fe^{3+} in the samples were calculated on the basis of the molar ratio of Zn to Fe as determined by ICP-AES and the chemical composition of Zn-doped Fe_3O_4 as $Zn_xFe^{2+}{}_{1-x}Fe^{3+}{}_2O_4$, which are listed in Table 2. The result as listed in Table 2 demonstrated that the molar ratio of Zn to Fe was affected by the addition of EDA. The saturation magnetization increased from 64.7 to 119 emu/g for E5 to E15, which is in direct proportion to the molar ratios of Fe to Zn and Fe^{2+} to Fe^{3+}. Zn^{2+} ions, which are nonmagnetic in nature, occupied tetrahedral sites (as A sites), and Fe^{3+} ions resided in octahedral sites (as B sites),[23,24] which

DOI: 10.1021/acs.jpcc.7b02084
J. Phys. Chem. C 2017, 121, 9612−9620

weakened the A−O−B interaction because of the dilution of spin moments and induced the saturation magnetization decrease. However, E20 obviously does not follow this change. To study this change, XPS spectra were determined for samples E10, E15, and E20 as shown in Figure 11. The analysis for XPS

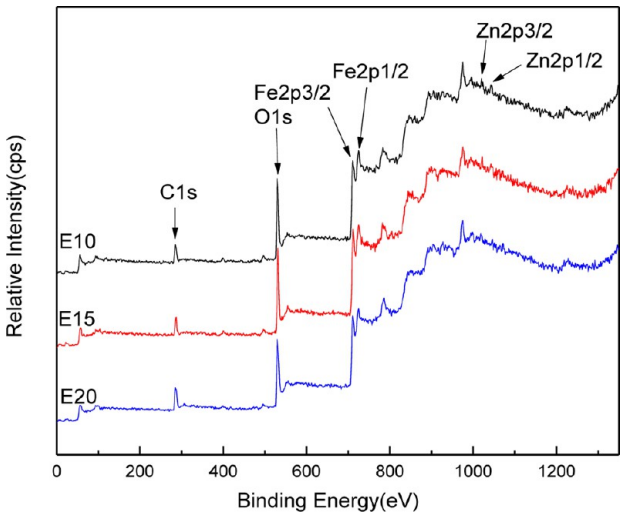

Figure 11. XPS survey spectra of the samples.

is listed in the Supporting Information as Figures S5−S7. From the XPS data, the occupation formula for samples E10, E15, and E20 are the following: $(Zn^{2+}_{0.104}Fe^{3+}_{0.896})_A[Fe^{2+}_{0.896}Fe^{3+}_{1.104}]_BO_4$, $(Zn^{2+}_{0.068}Fe^{3+}_{0.932})_A[Fe^{2+}_{0.932}Fe^{3+}_{1.068}]_BO_4$ and $(Zn^{2+}_{0.050}Fe^{3+}_{0.950})_A[Zn^{2+}_{0.032}Fe^{2+}_{0.918}Fe^{3+}_{1.050}]_BO_4$, respectively. For sample E20, Zn^{2+} ions partially substitute for Fe^{3+} ions at B sites, which reduced the magnetic moment of B sites and resulted in the net magnetic moment decrease. The molar ratio of Fe^{2+} to Fe^{3+} at the surface of the samples was calculated on the basis of XPS and is listed in Table S1, which is higher than those representing the composition of the sample based on the ICP-AES as listed in Table 2. Octahedral sites are preferentially exposed on the spinel surfaces.[25]

The temperature dependency of the zero-field-cooled (ZFC) and field-cooled (FC) magnetizations of samples E15 and E20 is shown in Figure 12. The magnetization increases in ZFC curves with the temperature increasing up to a certain value, which is called the blocking temperature (T_B). The plots of ZFC−FC magnetization show thermomagnetic irreversibility (divergence between FC and ZFC magnetization). This is the property of all magnetic systems exhibiting magnetic hysteresis behavior. The temperature at which the ZFC and FC curves begin to separate (T_{irr}) corresponds to the blocking or unblocking temperature of the largest particles. T_B and T_{irr} values are listed in Table 3, where T_{irr} represents the blocking

Table 3. Summary of Magnetic Parameters for the Samples

	T_B (K)	T_{irr} (K)
E15	200	~300
E20	190	~300

temperature of particles with the highest energy barrier and T_B gives the average value of the blocking temperatures of all of the particles. The result shows thermomagnetic irreversibility ($M_{FC} > M_{ZFC}$) below a certain temperature T_{irr} (~300 K), which reveals that the systems are in a blocked state for all temperatures below the mentioned one.[26] The difference between T_B and T_{irr} corresponds to the width of the blocking temperature distributions, and it also gives information regarding the grain size distributions in the samples.[27]

The zero-field ^{57}Fe Mössbauer spectra recorded at room temperature are shown in Figure 13 for samples E15 and E20. The computed hyperfine parameters are listed in Table 4. It can be found that the spectra exhibit a superposition of two Zeeman sextets for samples E15 and E20. The spectrum of compounds with the spinel structure is fitted using two sextets denoted as A and B sites, in which the fractions of iron ions are directly determined by the relative area ratios of the subspectra of corresponding A and B, respectively.[28] The outer sextet corresponding to a higher magnetic field (H_A) is attributed to Fe^{3+} at the A site, and the inner sextet corresponding to the lower magnetic field (H_B) is from Fe^{2+} and Fe^{3+} ions at the B site. The molar ratios of Fe^{3+} at the A site to B site were calculated to be about 0.67 and 0.78 for E15 and E20, respectively, which were about 0.81 and 0.85 by XPS.

The N_2 adsorption−desorption isotherms for samples E5−E20 are shown in Figure 14. The isotherm is of type IV and

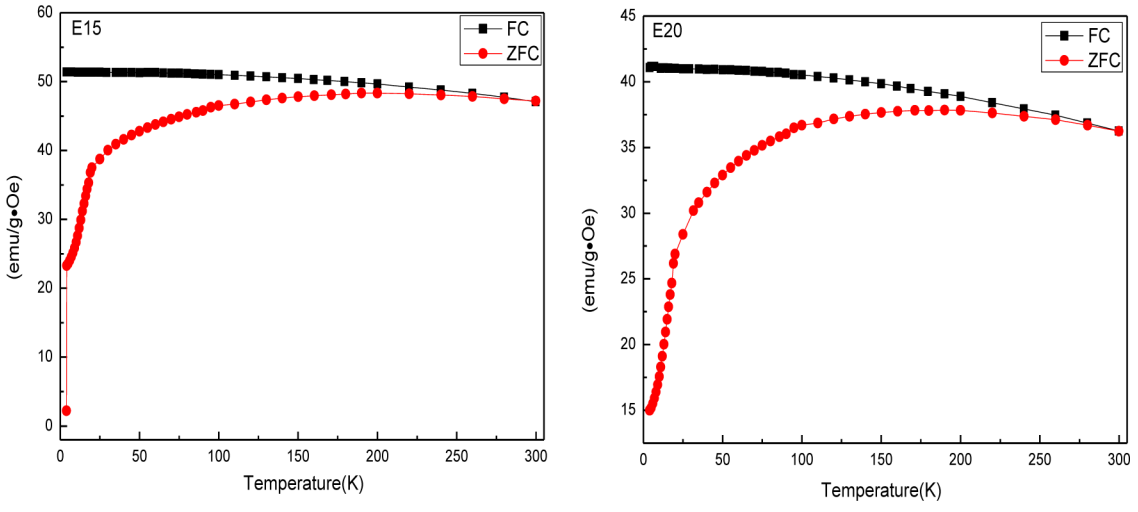

Figure 12. Zero-field-cooling and field-cooling curves of samples.

DOI: 10.1021/acs.jpcc.7b02084
J. Phys. Chem. C 2017, 121, 9612−9620

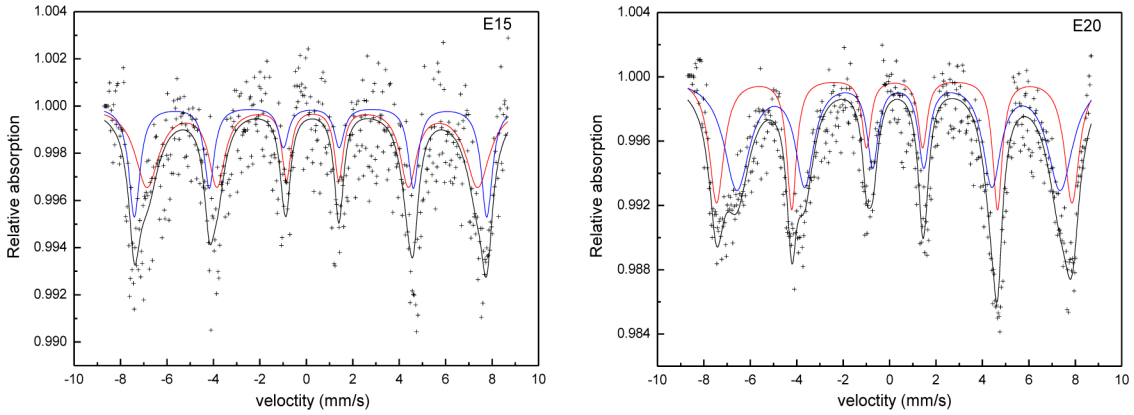

Figure 13. Mössbauer spectra of samples E15 and E20 at room temperature.

Table 4. Mössbauer Parameters for Samples E15 and E20

sample	IS (mm/s)	QS (mm/s)	H_f (T)	ARE (%)	site
E15	0.30	−0.03	47.1	40	A
	0.38	−0.01	44.3	60	B
E20	0.30	−0.00	47.4	44	A
	0.50	0.03	43.3	56	B

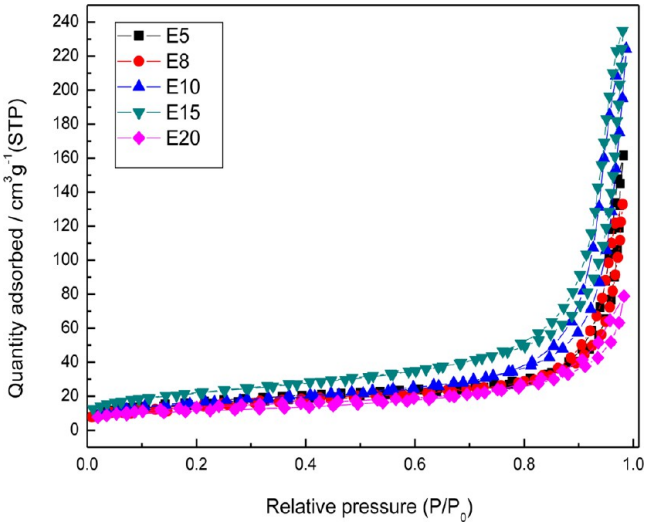

Figure 14. BET analysis for the samples.

displays the H3 hysteresis loop. According to the BET analysis, the BET surface area is shown in Table 5. The BET surface area

Table 5. Surface Area of the Samples

	E5	E8	E10	E15	E20
BET surface area (m^2/g)	60.8	54.0	60.6	80.6	49.3

of sample E15 was 80.6 m^2/g, which has a higher surface area than some samples with surface areas of 28,[29] 25.94,[30] and 74 m^2/g.[31] A large surface area can be obtained with dispersed nanoparticles.[32]

CONCLUSIONS

Zn-doped Fe_3O_4 magnetic nanosheets with a high magnetization and a large surface area were synthesized by a facile one-step solvothermal method. The Zn-doped Fe_3O_4 magnetic nanosheet formation mechanism was studied in detail using an in situ calorimetric method. Complex formation of $[Fe(EDA)_3]^{3+}$ and $[Zn(EDA)_3]^{2+}$ deceased the free Fe^{3+} and Zn^{2+} concentrations, which prevented some reactions and induced some reactions to occur at higher temperature. At the same time, the (111) facets of Zn-doped Fe_3O_4 became stable, which induced nanosheet formation. These results demonstrated that EDA can change the sample formation mechanism. The Zn-doped Fe_3O_4 nanosheets with a large saturation magnetization and a high surface area show potential applications in different fields such as adsorption, biomolecular separations, and targeted drug delivery.

ASSOCIATED CONTENT

Supporting Information

The Supporting Information is available free of charge on the ACS Publications website at DOI: 10.1021/acs.jpcc.7b02084.

TG/DTG curves of the samples under N_2, Fe $2p_{3/2}$ and Fe $2p_{1/2}$ XPS spectra, O 1s XPS spectra, Zn 2p XPS spectra, and results obtained from XPS spectra and composition at the A and B sites (PDF)

AUTHOR INFORMATION

Corresponding Author

*E-mail: zdnan@yzu.edu.cn. Tel: +86-514-87959896. Fax: +86-514-87959896.

ORCID

Zhaodong Nan: 0000-0001-8890-6795

Notes

The authors declare no competing financial interest.

ACKNOWLEDGMENTS

The authors gratefully acknowledge the financial support from the National Nature Science Foundations of China (21673204 and 21273196) and the Priority Academic Program Development of Jiangsu Higher Education Institutions.

REFERENCES

(1) Sakellari, D.; Brintakis, K.; Kostopoulou, A.; Myrovali, E.; Simeonidis, K.; Lappas, A. Ferrimagnetic Nanocrystal Assemblies as Versatile Magnetic Particle Hyperthermia Mediators. *Mater. Sci. Eng., C* **2016**, *58*, 187−193.

(2) Wang, D.; Zhou, W.; Zhang, Y.; Wang, Y.; Wu, G.; Yu, K.; Wen, G. A Novel One-step Strategy Toward $ZnMn_2O_4$/N-doped Graphene Nanosheets with Robust Chemical Interaction for Superior Lithium Storage. *Nanotechnology* **2016**, *27*, 04540.

DOI: 10.1021/acs.jpcc.7b02084
J. Phys. Chem. C 2017, 121, 9612−9620

(3) Tan, J.; Wan, J.; Guo, J.; Wang, C. Self-sacrificial Template-induced Modulation of Conjugated Microporous Polymer Microcapsules and Shape-dependent Enhanced Photothermal Efficiency for Ablation of Cancer Cells. *Chem. Commun.* **2015**, *51*, 17394−17397.
(4) Wang, W.; Zang, C.; Jiao, Q. Synthesis, Structure and Electromagnetic Properties of Mn-Zn Ferrite by Sol−gel Combustion Technique. *J. Magn. Magn. Mater.* **2014**, *349*, 116−120.
(5) Liang, J.; Ma, H.; Luo, W.; Wang, S. Synthesis of Magnetite Submicrospheres with Tunable Size and Superparamagnetism by A Facile Polyol Process. *Mater. Chem. Phys.* **2013**, *139*, 383−388.
(6) Luo, B.; Xu, S.; Luo, A.; Wang, W. R.; Wang, S. L.; Guo, J. Mesoporous Biocompatible and Acid-degradable Magnetic Colloidal Nanocrystal Clusters with Sustainable Stability and High Hydrophobic Drug Loading Capacity. *ACS Nano* **2011**, *5*, 1428−1435.
(7) Xuan, S.; Wang, F.; Wang, Y. X. J.; Yu, J. C.; Leung, C. F. Facile Synthesis of Size-controllable Monodispersed Ferrite Nanospheres. *J. Mater. Chem.* **2010**, *20*, 5086−5094.
(8) Yuan, Y.; Chen, L.; Yang, R.; Lu, X.; Peng, H.; Luo, Z. Solid-state Synthesis and Characterization of Core-shell $CoFe_2O_4$-carbon Composite Nanoparticles from A Heterometallic Trinuclear Complex. *Mater. Lett.* **2012**, *71*, 123−126.
(9) Tang, Y.; Liu, Y.; Li, W.; Xie, Y.; Li, Y.; Wu, J. Synthesis of Sub-100 nm Biocompatible Superparamagnetic Fe_3O_4 Colloidal Nanocrystal Clusters as Contrast Agents for Magnetic Resonance Imaging. *RSC Adv.* **2016**, *6*, 62550−62555.
(10) Liu, J.; Bin, Y. Z.; Matsuo, M. Magnetic Behavior of Zn-doped Fe_3O_4 Nanoparticles Estimated in Terms of Crystal Domain Size. *J. Phys. Chem. C* **2012**, *116*, 134−143.
(11) Park, J.; Jin, J.; Kwon, S. G.; Jang, Y.; Hyeon, T. Synthesis of Monodisperse Spherical Nanocrystals. *Angew. Chem., Int. Ed.* **2007**, *46*, 4630−4660.
(12) Yin, Y.; Alivisatos, A. P. Colloidal Nanocrystal Synthesis and The Organic-inorganic Interface. *Nature* **2005**, *437*, 664−670.
(13) Ding, Y.; Liu, F.; Jiang, Q.; Du, B.; Sun, H. 12-hydrothermal Synthesis and Characterization of Fe_3O_4 Nanorods. *J. Inorg. Organomet. Polym. Mater.* **2013**, *22*, 379−384.
(14) Zhu, L. P.; Xiao, H. M.; Zhang, W. D.; Yang, Y.; Fu, S. Y. Synthesis and Characterization of Novel Three-dimensional Metallic Co Dendritic Superstructures by A Simple Hydrothermal Reduction Route. *Cryst. Growth Des.* **2008**, *8*, 1113−1118.
(15) Liu, J.; Zhang, Y.; Nan, Z. Facile Synthesis of Stoichiometric Zinc Ferrite Nanocrystal Clusters with Superparamagnetism and High Magnetization. *Mater. Res. Bull.* **2014**, *60*, 270−278.
(16) Zhao, B.; Nan, Z. One-pot Synthesis of $ZnLa_xFe_{2-x}O_4$ Clusters without any Template and Their Possible Application in Water Treatment. *J. Mater. Chem.* **2012**, *22*, 6581−6586.
(17) Liu, X.; Liu, J.; Zhang, S.; Nan, Z.; Shi, Q. Structural, Magnetic, and Thermodynamic Evolutions of Zn-doped Fe_3O_4 Nanoparticles Synthesized Using A One-step Solvothermal Method. *J. Phys. Chem. C* **2016**, *120*, 1328−1341.
(18) Prasad, B. D.; Nagabhushana, H.; Thyagarajan, K.; Nagabhushana, B. M.; Jnaneshwara, D. M.; Sharma, S. C. Temperature Dependent Magnetic Ordering and Electrical Transport Behavior of Nano Zinc Ferrite from 20 to 800K. *J. Alloys Compd.* **2014**, *590*, 184−192.
(19) Rameshbabu, R.; Ramesh, R.; Kanagesan, S.; Karthigeyan, A.; Ponnusamy, S. Synthesis and Study of Structural, Morphological and Magnetic Properties of $ZnFe_2O_4$ Nanoparticles. *J. Supercond. Novel Magn.* **2014**, *27*, 1499−1502.
(20) Barick, K. C.; Aslam, M.; Lin, Y. P.; Bahadur, D.; Prasad, P. V.; Dravid, V. P. Novel and Efficient MR Active Aqueous Colloidal Fe_3O_4 Nanoassemblies. *J. Mater. Chem.* **2009**, *19*, 7023−7029.
(21) Liu, J.; Nan, Z.; Gao, S. In Situ Microcalorimetry Study of $ZnFe_2O_4$ Nanoparticle Formation under Solvothermal Conditions. *Dalton T.* **2015**, *44*, 17293.
(22) Zhao, H.; Liu, R.; Zhang, Q.; Wang, Q. Effect of Surfactant Amount on The Morphology and Magnetic Properties of Monodisperse $ZnFe_2O_4$ Nanoparticles. *Mater. Res. Bull.* **2016**, *75*, 172−177.
(23) Najmoddin, N.; Beitollahi, A.; Devlin, E.; Kavas, H.; Mohseni, S. M.; Åkerman, J. Magnetic Properties of Crystalline Mesoporous Zn-substituted Copper Ferrite Synthesized under Nanoconfinement in Silica Matrix. *Microporous Mesoporous Mater.* **2014**, *190*, 346−355.
(24) Ibrahim, I.; Ali, I. O.; Salama, T. M.; Bahgat, A. A.; Mohamed, M. M. Synthesis of Magnetically Recyclable Spinel Ferrite (MFe_2O_4, M= Zn, Co, Mn) Nanocrystals Engineered by Sol Gel-hydrothermal Technology: High Catalytic Performances for Nitroarenes Reduction. *Appl. Catal., B* **2016**, *181*, 389−402.
(25) Jacobs, J. P.; Maltha, A.; Reintjes, J. G. H.; Drimal, J.; Ponec, V.; Brongersma, H. H. The Surface of Catalytically Active Spinels. *J. Catal.* **1994**, *147*, 294−300.
(26) Ferrari, S.; Aphesteguy, J. C.; Saccone, F. D. Structural and Magnetic Properties of Zn Doped Magnetite Nanoparticles Obtained by Wet Chemical Method. *IEEE Trans. Magn.* **2014**, *51*, 1−6.
(27) Cannas, C.; Casula, M. F.; Concas, G.; Corrias, A.; Gatteschi, D.; Falqui, A. Magnetic Properties of γ-Fe_2O_3-SiO_2 Aerogel and Xerogel Nanocomposite Materials. *J. Mater. Chem.* **2001**, *11*, 3180−3187.
(28) Wang, J.; Wu, H. Y.; Yang, C. Q.; Lin, Y. L. Room Temperature Mössbauer Characterization of Ferrites with Spinel Structure. *Mater. Charact.* **2008**, *59*, 1716−1720.
(29) Wang, Q.; Deng, J.; Sun, J.; Shu, C. M.; Luo, Z.; Liu, B. Flame Propagation Characteristics and Combustion Mechanism of FeOOH-coated Zirconium Particles. *J. Therm. Anal. Calorim.* **2012**, *126*, 1−9.
(30) Xin, X.; Wei, Q.; Yang, J.; Yan, L.; Feng, R.; Chen, G. Highly Efficient Removal of Heavy Metal Ions by Amine-functionalized Mesoporous Fe_3O_4 Nanoparticles. *Chem. Eng. J.* **2012**, *184*, 132−140.
(31) Khosravi, M.; Azizian, S. Synthesis of Fe_3O_4 Flower-like Hierarchical Nanostructures with High Adsorption Performance Toward Dye Molecules. *Colloids Surf., A* **2015**, *482*, 438−446.
(32) Ismail, A. A.; Bahnemann, D. W. Mesoporous Titania Photocatalysts: Preparation, Characterization and Reaction Mechanisms. *J. Mater. Chem.* **2011**, *21*, 11686−11707.

DOI: 10.1021/acs.jpcc.7b02084
J. Phys. Chem. C 2017, 121, 9612−9620